

# Extending the Concept of Probability Flux

Douglas J. Mason, Mario F. Borunda, and Eric J. Heller  
*Department of Physics, Harvard University, Cambridge, MA 02138, USA*  
(Dated: 05/16/12)

We develop the Husimi map for visualizing quantum wavefunctions using coherent states as a measurement of the local phase space to produce a vector field related to the probability flux. Adapted from the Husimi projection, the Husimi map is complimentary to the usual flux map, since they are identical for small coherent states. By improving our understanding of the flux operator and offering a robust and flexible alternative, we show how the Husimi projection can provide a map to the classical dynamics underlying a quantum wavefunction. We demonstrate its capabilities on bound systems with electromagnetic fields, as well as on open systems on and off resonance.

## I. INTRODUCTION

The probability flux, or probability current, is introduced in quantum mechanics textbooks as a deterministic operator that can be calculated, but its connection to experiment is often left to the reader's imagination. The flux operator, whose expectation over the wavefunction gives the traditional flux  $\mathbf{j}(\mathbf{r}, \mathbf{p})$ , is defined as

$$\hat{\mathbf{j}}_{\mathbf{r}} = \frac{1}{2m} (|\mathbf{r}\rangle \langle \mathbf{p} | \hat{\mathbf{p}} + \hat{\mathbf{p}} | \mathbf{r}\rangle \langle \mathbf{r} |), \quad (1)$$

where  $m$  is the mass of a particle in the system, and  $\mathbf{r}$  and  $\mathbf{p}$  the position and momentum. The concept of “flux at a point” seems paradoxical because we say something about momentum while also knowing position precisely. This raises the question: Can the flux even be measured?

On the other hand, probability flux vanishes on stationary states for systems with time-reversal symmetry. This is a shame, since strong semiclassical connections between trajectory flow and quantum eigenstates lie completely hidden in the universal value of 0 for the flux. Consider the example in Fig. 1, where the strong influence of classical orbits is seen in the scarred eigenstate[1]. For this bound system, the flux is always zero, but when it is coupled to a continuum, flux becomes useful as a tool for examining its dynamics, even though information about the dynamics clearly exists before the coupling. Is

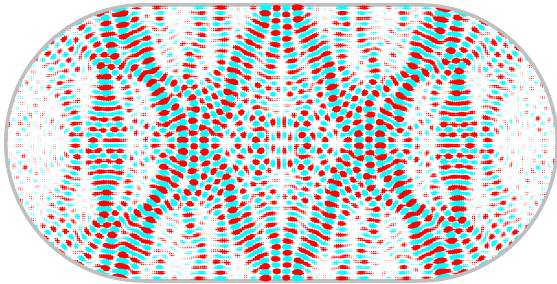


Figure 1: A scarred eigenstate of the stadium billiard problem is a particle in a box with the shape shown, revealing the strong influence of classical orbits. The traditional flux provides no help: it is uniformly 0 inside the billiard.

it possible to bridge this gap?

By using coherent state projections, also known as Husimi projections[2], we can reveal the meaning of the flux operator *and* see how to extend it to become much more useful. The experimental equivalent of a flux map has not been discussed because it is effectively impossible to measure – determining the flux, even at a single point, requires an infinite number of measurements. Instead, we offer an experimentally feasible extension of the flux operator based on Husimi projections which produces identical results to the traditional flux (Eq. 1) in the limit of infinitesimal coherent states. Because the Husimi projection is able to work away from this limit and on a wider variety of systems, it is able to bridge the gap between stationary and scattering states and identify conductance pathways in large transport systems.

When many Husimi projections are sampled across a system, they produce a Husimi *map* which is a powerful tool for interpreting the semiclassical behavior of wavefunctions. In addition to showing the locations and directions of classical trajectories suggested by a wavefunction, Husimi maps can also quantify how boundaries and external fields affect those trajectories. Previous work laid out the foundation for extending the flux operator using the Husimi projection[3]. In this paper, we present a complete discussion of the results summarized there and demonstrate Husimi maps on a wider variety of systems with and without external fields. We then show how to use Husimi maps to interpret flux through various open devices.

## II. MEASUREMENT AND THE FLUX OPERATOR

### A. The Gaussian Basis

Several discussions connecting the flux to experimental measurement exist in the literature[4–6]; here we offer an alternative view. We begin by identifying the eigenstates of the flux operator and giving them a physical interpretation.

When discussing uncertainty, the Dirac basis implicit

in Eq. 1 introduces singularities which we can avoid by replacing the delta functions with the Gaussian basis defined as

$$\langle \mathbf{r} | \mathbf{r}_0, \sigma \rangle = \left( \frac{1}{\sigma \sqrt{\pi/2}} \right)^{d/2} e^{-(\mathbf{r}-\mathbf{r}_0)^2/4\sigma^2}, \quad (2)$$

where  $d$  is the number of dimensions in the system. The Gaussian function becomes a delta function as  $\sigma \rightarrow 0$ . In the Gaussian basis, the flux operator is

$$\hat{j}_{\mathbf{r}_0, \sigma} = \frac{1}{2m} (|\mathbf{r}_0, \sigma\rangle \langle \mathbf{r}_0, \sigma| \hat{\mathbf{p}} + \hat{\mathbf{p}} |\mathbf{r}_0, \sigma\rangle \langle \mathbf{r}_0, \sigma|). \quad (3)$$

The eigenstates, projected onto each orthogonal spatial dimension  $i$ , are obtained using the eigenvalue equation

$$\hat{j}_{\mathbf{r}_0, \sigma, i} |\lambda_{\sigma, i}\rangle = \lambda_{\sigma, i} |\lambda_{\sigma, i}\rangle, \quad (4)$$

which has a solution of the form

$$|\lambda_{\sigma, i}\rangle = |\mathbf{r}_0, \sigma\rangle + a \hat{p}_i |\mathbf{r}_0, \sigma\rangle. \quad (5)$$

Using the two equations

$$\langle \mathbf{r} | \hat{\mathbf{p}} | \mathbf{r}_0, \sigma \rangle = i\hbar\sigma^{-2} (\mathbf{r} - \mathbf{r}_0) e^{-(\mathbf{r}-\mathbf{r}_0)^2/2\sigma^2} \quad (6)$$

and

$$\langle \mathbf{r}_0, \sigma | \hat{\mathbf{p}} | \mathbf{r}_0, \sigma \rangle = 0, \quad (7)$$

we can write

$$\hat{j}_{\mathbf{r}_0, \sigma, i} |\lambda_{\sigma, i}\rangle = \frac{1}{2m} (a \langle \hat{p}_i^2 \rangle_\sigma |\mathbf{r}_0, \sigma\rangle + \hat{p}_i |\mathbf{r}_0, \sigma\rangle). \quad (8)$$

Further, it is useful to find the conditions on  $\lambda_{\sigma, i}$  that allow Eq. 8 to be written in the form of Eq. 4,

$$\lambda_{\sigma, i} = \frac{a}{2m} \langle \hat{p}_i^2 \rangle_\sigma; \lambda_{\sigma, i} = \frac{1}{2ma}. \quad (9)$$

Since  $\langle \hat{p}_i^2 \rangle_\sigma = \frac{\hbar^2}{4\sigma^2}$ , the value of  $a$  can be determined and from that we obtain the two eigenvalues

$$\lambda_{\sigma, i, \pm} = \pm \frac{\hbar}{4m\sigma}. \quad (10)$$

The eigenstates take the form

$$\langle \mathbf{r} | \lambda_{\sigma, i, \pm} \rangle = \langle \mathbf{r} | \mathbf{r}_0, \sigma \rangle \pm \frac{i}{\sigma} \mathbf{e}_i \cdot (\mathbf{r} - \mathbf{r}_0) \langle \mathbf{r} | \mathbf{r}_0, \sigma \rangle, \quad (11)$$

where  $\mathbf{e}_i$  is the unit vector along spatial dimension  $i$ . Eq. 11 is a linear combination of two functions: the Gaussian (Eq. 2) and its derivative. Projection of a wavefunction onto the first term can be interpreted as measuring its probability amplitude at point  $\mathbf{r}_0$ , and projection onto the second term as measuring its derivative along the  $i^{\text{th}}$  spatial dimension at the point  $\mathbf{r}_0$ .

Because there are two eigenstates along each spatial dimension, we show in Appendix A that determining the

flux expectation value on a wavefunction  $\psi(\mathbf{r})$  equates to calculating two dot products according to

$$\begin{aligned} \langle \psi | \hat{j}_{\mathbf{r}_0, \sigma, i} | \psi \rangle &= \lambda_{\sigma, i, +} |\langle \psi | \lambda_{\sigma, i, +} \rangle|^2 \\ &\quad + \lambda_{\sigma, i, -} |\langle \psi | \lambda_{\sigma, i, -} \rangle|^2 \end{aligned} \quad (12)$$

Eq. 12 can be rewritten as

$$\begin{aligned} \langle \psi | \hat{j}_{\mathbf{r}_0, \sigma, i} | \psi \rangle &= \frac{i\hbar}{4m\sigma^2} [\langle \psi | \mathbf{e}_i \cdot (\mathbf{r} - \mathbf{r}_0) | \mathbf{r}_0, \sigma \rangle \langle \psi | \mathbf{r}_0, \sigma \rangle^* \\ &\quad - \langle \psi | \mathbf{e}_i \cdot (\mathbf{r} - \mathbf{r}_0) | \mathbf{r}_0, \sigma \rangle^* \langle \psi | \mathbf{r}_0, \sigma \rangle] \end{aligned} \quad (13)$$

The traditional flux operator arises from the limit  $\sigma \rightarrow 0^+$ , at which point the two terms in Eq. 11 become the delta function and its derivative, while the flux values of the first eigenstates become

$$\lim_{\sigma \rightarrow 0^+} \lambda_{\sigma, i, \pm} = \pm \infty. \quad (14)$$

In addition, there are an infinite number of other eigenstates with zero eigenvalues (See Appendix A). As a result, a single application of the flux at a particular point in space  $\hat{j}_{\mathbf{r}_0, i}$  almost always results in zero, but occasionally in an extremely large positive or negative value. Traditionally, measurements of the flux correspond to the application of the operator and averaging the results. Performing the averaging over an infinite number of measurements results in the expression equivalent to the textbook flux.

## B. Connection to Coherent States

The prefactors before the Gaussian states in Eq. 11 are related to the Taylor expansion

$$e^{\pm \frac{i}{\sigma} \mathbf{e}_i \cdot (\mathbf{r} - \mathbf{r}_0)} \approx 1 \pm \frac{i}{\sigma} \mathbf{e}_i \cdot (\mathbf{r} - \mathbf{r}_0). \quad (15)$$

This suggests there may be a deep connection between the flux eigenstates and the coherent state, defined as

$$\langle \mathbf{r} | \mathbf{r}_0, \mathbf{k}_0, \sigma \rangle = \left( \frac{1}{\sigma \sqrt{\pi/2}} \right)^{d/2} e^{-(\mathbf{r}-\mathbf{r}_0)^2/4\sigma^2 + i\mathbf{k}_0 \cdot \mathbf{r}}, \quad (16)$$

which is a Gaussian envelope over a plane wave  $e^{i\mathbf{k}_0 \cdot \mathbf{r}}$ . Its inner product with a generic wavefunction  $\psi(\mathbf{r})$  is

$$\begin{aligned} \langle \psi | \mathbf{r}_0, \mathbf{k}_0, \sigma \rangle &= \left( \frac{1}{\sigma \sqrt{\pi/2}} \right)^{d/2} \\ &\quad \times \int \psi(\mathbf{r}) e^{-(\mathbf{r}-\mathbf{r}_0)^2/4\sigma^2 + i\mathbf{k}_0 \cdot \mathbf{r}} d^d r \end{aligned} \quad (17)$$

Observing that the phase  $e^{i\mathbf{k}_0 \cdot \mathbf{r}_0}$  is arbitrary, we can Taylor expand the exponential function in the limit of  $\mathbf{k}_0 \sigma \ll 1$  to produce

$$\begin{aligned}
\langle \mathbf{r} | \mathbf{r}_0, \mathbf{k}_0, \sigma \rangle &\approx \left( \frac{1}{\sigma \sqrt{\pi/2}} \right)^{d/2} e^{-(\mathbf{r}-\mathbf{r}_0)^2/4\sigma^2} \\
&\times (1 + i\mathbf{k}_0 \cdot (\mathbf{r} - \mathbf{r}_0)) \quad (18) \\
&\approx \langle \mathbf{r} | \mathbf{r}_0, \sigma \rangle + i\mathbf{k}_0 \cdot (\mathbf{r} - \mathbf{r}_0) \langle \mathbf{r} | \mathbf{r}_0, \sigma \rangle \quad (19)
\end{aligned}$$

Note that the dispersion relation for the free-particle continuum is a circle with radius  $k_0 = \frac{\sqrt{2mE}}{\hbar}$ , which is independent of the orientation of  $\mathbf{k}_0$ . The second term in Eq. 19 is thus proportional to the second term in Eq. 11 for  $\mathbf{k}_0$  projected along the  $i^{\text{th}}$  dimension. The similarity in form between Eq. 19 and Eq. 11 allows us to relate the flux expectation value from Eqs. 12 and 13 to coherent state projections as

$$\lim_{\sigma k_0 \rightarrow 0} \langle \psi | \hat{j}_{\mathbf{r}_0, \sigma, i} | \psi \rangle = \frac{\hbar k_0}{4m\sigma^2} [|\langle \psi | \mathbf{r}_0, k_0 \mathbf{e}_i, \sigma \rangle|^2 - |\langle \psi | \mathbf{r}_0, -k_0 \mathbf{e}_i, \sigma \rangle|^2]. \quad (20)$$

The traditional flux *vector* is constructed from the components in each direction.

Unlike the Gaussian states appearing in the flux eigenstates in Eq. 11, the physical meaning of coherent states is straightforward: they describe a semiclassical particle minimizing the product of position and momentum uncertainties. By the well-known uncertainty relation

$$\Delta x \propto \frac{1}{\Delta k} \propto \sigma, \quad (21)$$

taking  $\sigma \rightarrow 0$  results in coherent state measurements with infinite uncertainty in  $k$ -space, and zero uncertainty in real space. This is the limit where the traditional flux operates.

### C. Definition of the Husimi Projection

The properties of coherent states make them a suitable basis for expanding the flux operator to a measurable definition, which we call the Husimi function[2]. It is defined as a measurement of a wavefunction  $\psi(\mathbf{r})$  by a coherent state, or “test wavepacket”, written as

$$\text{Hu}(\mathbf{r}_0, \mathbf{k}_0, \sigma; \psi(\mathbf{r})) = |\langle \psi | \mathbf{r}_0, \mathbf{k}_0, \sigma \rangle|^2. \quad (22)$$

Weighting each of these measurements by the wavevector produces a Husimi vector; plotting all Husimi vectors at a point produces the full Husimi projection. These projections are the sunbursts in Fig. 2, which shows Husimi projections for the wavefunctions

$$\begin{aligned}
\Psi_A(\mathbf{r}) &= e^{i\mathbf{k}_1 \cdot \mathbf{r}} \\
\Psi_B(\mathbf{r}) &= \cos(\mathbf{k}_1 \cdot \mathbf{r}), \quad (23)
\end{aligned}$$

where  $\mathbf{k}_1$  points towards the upper-right. We show the wavevectors that generate each state in the white arrow overlay.

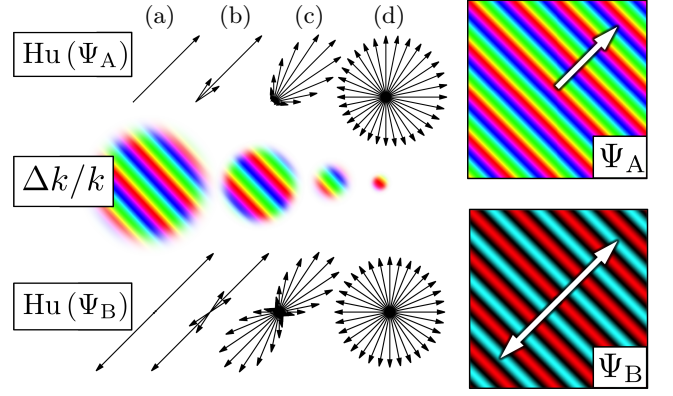


Figure 2: Husimi vectors for 32 equally-space points in  $k$ -space at left for the two wavefunctions at right: the complex plane wave ( $\Psi_A$ ) and the cosine wave ( $\Psi_B$ ) defined in Eq. 23. The uncertainty for each projection corresponds to  $\Delta k/k = 2\%$ (a),  $10\%$ (b),  $50\%$ (c),  $250\%$ (d), corresponding to smaller wavepacket spreads (middle) and less distinction between independent measurements (top and bottom). Above, we represent the coherent wavepacket spread using schematic circles; in general, we indicate the spread using double-arrows.

Both wavefunctions are pure momentum states which are not spatially localized, and constitute the building blocks for the wavefunctions addressed in this paper. The plane wave  $\Psi_A$  is relevant to magnetic field states discussed in Section III B. The cosine wave  $\Psi_B$  corresponds to time-reversal symmetric wavefunctions discussed in Sections III A and III C. Both  $\Psi_A$  and  $\Psi_B$  are important for scattering wavefunctions presented in Section IV A which exhibit a mixture of both properties.

Because of the large momentum uncertainty for small  $\sigma$ , coherent state projections merely reproduce the probability amplitude  $|\psi(\mathbf{r})|^2$  in all directions of  $\mathbf{k}_0$ , as seen in Fig. 2d. The flux emerges as a small residual which can be retrieved by summing each coherent state projection weighted by  $\mathbf{k}_0$ . We call this quantity the vector-valued Husimi flux,

$$\mathbf{Hu}(\mathbf{r}_0, \sigma; \psi(\mathbf{r})) = \int \mathbf{k}_0 |\langle \psi | \mathbf{r}_0, \mathbf{k}_0, \sigma \rangle|^2 d^d k_0. \quad (24)$$

In Appendix B, we show that as  $\sigma \rightarrow 0$ , the contributing points in the integral over  $k$ -space reduce to just the orthogonal directions. In this limit, we can write the Husimi flux as

$$\lim_{\sigma \rightarrow 0} \mathbf{Hu}(\mathbf{r}_0, \sigma; \psi(\mathbf{r})) \propto \sum_{i=1}^d \mathbf{e}_i [|\langle \psi | \mathbf{r}_0, k_0 \mathbf{e}_i, \sigma \rangle|^2 - |\langle \psi | \mathbf{r}_0, -k_0 \mathbf{e}_i, \sigma \rangle|^2], \quad (25)$$

where  $\mathbf{e}_i$  is the unit vector along the  $i^{\text{th}}$  orthogonal direction, and we sum over  $d$  dimensions. By Eq. 20, both sides of Eq. 25 are proportional to the traditional flux measured at point  $\mathbf{r}_0$  so that

$$\langle \psi | \hat{\mathbf{j}}_{\mathbf{r}_0} | \psi \rangle \propto \lim_{\sigma \rightarrow 0} \mathbf{H}\mathbf{u}(\mathbf{r}_0, \sigma; \psi). \quad (26)$$

For larger  $\sigma$ , reduced momentum uncertainty allows for substantial variation in the coherent state projections between different directions of  $\mathbf{k}_0$ . This can be seen in Fig. 2 as uncertainty is reduced and uniform sunbursts (d) contract into lobes (c), and finally to unambiguous vectors (a-b). At all uncertainties, the absence of flux in time-reversal symmetric states can be interpreted as the perfect cancelation of coherent state projections along each direction in  $k$ -space. The equal participation of counter-propagating flux while absent in  $\Psi_A$  is evident in  $\Psi_B$  as a reflected sunburst.

The reduced momentum uncertainty for larger coherent states also reduces spatial resolution. In the intermediate regime, we can use Husimi projections to map the local phase space of a wavefunction. By taking snapshots of the local phase space at many points across a system for larger  $\sigma$ , we can produce a map of the classical trajectories that correspond to a given wavefunction. These visualizations are known as “Husimi maps”[2, 7–9]. Like the traditional flux map, Husimi maps can be integrated over lines and surfaces to reveal the total probability flux current.

To produce the Husimi map, we sample Husimi projections along a grid in spatial coordinates, since it is easier to plot, straightforward to interpret, and allows for computing spatial derivatives (see Section II E). However, other schemes may be preferred. In Fig. 5, for example, we sample along classical trajectories to emphasize the quantum-classical correspondence. While this paper addresses two-dimensional systems, Husimi projections are equally applicable for higher-dimensional systems.

Husimi maps also have implications for experiments since they could be measured in a fashion similar to angle-resolved photo-emission spectroscopy (ARPES), which is currently used to measure the dispersion relation and Fermi surfaces (for a review, see [10]). In the ARPES setup, a focused photon beam on a sample kicks off electrons in the valence band. The energy of the photo-emitted electrons incorporates both their bonding energies, which can be averaged over, and their kinetic energy, which depends on the angle of the beam with respect to the sample surface.

The ARPES response function behaves similarly to coherent state projections with  $\mathbf{k}_0$  proportional to the beam angle. By rotating the beam angle around the same point of intersection, the response in different directions provides the momentum distribution of the wavefunction at that point. Perturbations from the known dispersion relation can then be inserted into Eq. 24 to obtain the flux expectation value.

While a narrow beam would make it possible to measure the flux vector at the intersection point, it will be difficult to distinguish the occasional large perturbation measurements from noise. However, wider beams would

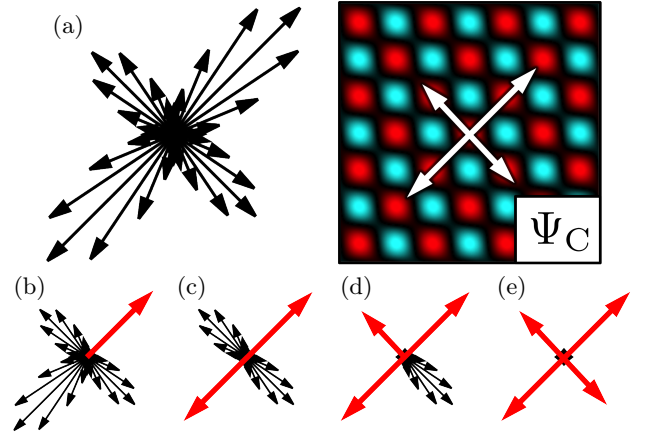


Figure 3: Husimi vectors for 32 equally-space points in  $k$ -space (a) for the double cosine waves ( $\Psi_C$ ) from Eq. 27. The uncertainty for each projection corresponds to  $\Delta k/k = 30\%$ . As the multi-modal algorithm (Algorithm 1) loops through each iteration (b-e), a trajectory is matched and then subtracted from the full Husimi projection, until all major trajectories are approximated by their appropriate values.

capture additional terms from the Taylor expansion of the coherent state in Eq. 19, producing more reliable perturbation measurements. Applying the technique at many points across the sample would then provide the Husimi map and an approximation to the flux map.

A question arises regarding the handling of boundaries in the system, beyond which the wavefunction goes to zero. Our definition reduces the magnitude of Husimi projections within distance  $\sigma$  of the boundary. When a coherent state interacts with a boundary, the boundary can be replaced by an image wavepacket moving in the opposite direction. In this case, reflections off the boundary amount to scattering between wavepackets with different wavevectors. Thus, the reduction in the Husimi projections near the boundaries is the result of wavepacket scattering, making it possible to use Husimi maps to compute scattering metrics along the boundary, such as angular deflection presented in Section II E.

#### D. Multi-Modal Analysis

The Husimi projections in Fig. 2 reveal that even a single plane wave produces a range of Husimi vectors because of the finite spread of the wavepacket. Can distinct trajectories intersecting at a point be distinguished unambiguously? If the dominant plane waves at a point are sufficiently separated in  $k$ -space, i.e. the momentum uncertainty of the coherent state can resolve between them, we can retrieve their wavevectors numerically using Multi-Modal Analysis (MMA). This analytical tool can be especially useful for time-reversal symmetric systems where both the traditional flux and the Husimi total flux are identically zero.



---

**Algorithm 1** Multi-Modal Analysis (MMA)

---

1. A set of Husimi templates on  $N$  wavevectors  $\{\mathbf{k}_j\}$  is created for the wavefunctions  $\Psi = e^{i\mathbf{k}_i^{\text{test}} \cdot \mathbf{r}}$  generated by the  $M$  wavevectors  $\{\mathbf{k}_i^{\text{test}}\}$ . Both sets of wavevectors lie along the dispersion contour. Each template can be stored as a vector of values  $\mathbf{u}_i$  of length  $M$  where each member corresponds to the Husimi function along the wavevector  $\mathbf{k}_j$ .
  2. Writing the Husimi projection as the vector  $\mathbf{v}$ , a metric is computed  $d_i = \mathbf{v} \cdot \mathbf{u}_i$  for each Husimi template.
  3. The maximum of the set  $\{d_i\}$  is determined, and both the wavevector  $\mathbf{k}_i^{\text{test}}$  and the dot product  $d_i$  are stored.
  4. The contribution of the trajectory with wavevector  $\mathbf{k}_i^{\text{test}}$  is determined by the re-weighted vector  $\mathbf{u}_i \frac{d_i}{\mathbf{u}_i \cdot \mathbf{u}_i}$ .
  5. The re-weighted template vector is subtracted from the projection, that is,  $\mathbf{v} \rightarrow \mathbf{v} - \mathbf{u}_i \frac{d_i}{\mathbf{u}_i \cdot \mathbf{u}_i}$ .
  6. All elements of  $\mathbf{v}$  which are now negative are set to zero.
  7. Steps 1-6 are repeated until the metric  $d_i$  dips below a threshold.
  8. The set of vectors  $\{d_i \mathbf{k}_i^{\text{test}}\}$  are used to approximate the Husimi projection
- 

Figs. 3 demonstrates the MMA algorithm on the pure momentum state

$$\Psi_C(\mathbf{r}) = \alpha \cos(\mathbf{k}_1 \cdot \mathbf{r}) + \beta \cos(\mathbf{k}_2 \cdot \mathbf{r}), \quad (27)$$

where  $\mathbf{k}_1$  points towards the upper-right and  $\mathbf{k}_2$  points towards the upper-left. We set  $\alpha = 1$  and  $\beta = 0.8$ . In Fig. 3a, the Husimi projection is shown with a sizable uncertainty of  $\Delta k/k = 30\%$ . Parts b-e iterate through the *for* loop in steps 1-6 of the MMA Algorithm. At each iteration, the most dominant plane wave in the sunburst is modeled and then subtracted from the projection. This is repeated until all major plane waves have been approximated. If the dominant trajectories intersecting at a point have sufficiently divergent momenta, not only does the algorithm do an excellent job of modeling them, it can even compute how many there are. In general, we stop the loop in Step 7 after a certain number of iterations to make clearer figures.

On the other hand, when there are a number of trajectories of equal weight whose momenta cannot be resolved by the coherent state, the MMA Algorithm can produce unexpected results. An example of unresolved trajectories is seen in the points sampled along the perimeter of Fig. 4a and in the central regions of Figs. 4b-d and 5. In these cases, the MMA Algorithm approximates overlapping trajectories by first choosing their average, and then contributing additional trajectories on either side.

When the traditional flux is non-trivial, as in Fig. 7 and magnified in Fig. 8a, it averages over trajectories at each point to produce the total drift flow. For this reason the multi-modal analysis is able to augment the information provided by the flux operator since it can show the individual trajectories contributing to the av-

erage. For example, in Sec. IIIB, we compare the drift flow highlighted by the flux to the classical paths and the multi-modal analysis for the same system.

### E. Angular Deflection

The Husimi map makes it possible to compute other quantities tied to the semiclassical underpinnings of a quantum wavefunction. This section, and the results examined in Section IIIC, focus on one: angular deflection, which reveals where system boundaries and external fields deflect classical trajectories from straight paths and give rise to the shape and properties of a given wavefunction.

We begin by considering the Husimi function for one point in  $k$ -space measured at equally-spaced points on a grid that covers the system. The scalar field yields a spatial map of the presence of an individual trajectory angle, and fluctuations in the map indicate points where classical paths deflect away from and towards the angle. Summing the results for all wavevectors along the contour line defined by system energy in the dispersion relation, we can derive a measurement of angular deflection  $Q_{\text{ang.}}(\mathbf{r}; \Psi)$  written as

$$Q_{\text{ang.}}(\mathbf{r}; \Psi) = \int D_{\text{abs.}}(\mathbf{r}, \mathbf{k}; \Psi) k d^d k. \quad (28)$$

$D_{\text{abs.}}(\mathbf{r}, \mathbf{k}; \Psi)$  is the Gaussian-weighted absolute divergence of the Husimi map for wavevector  $\mathbf{k}$  written as

$$D_{\text{abs.}}(\mathbf{r}, \mathbf{k}; \Psi) = \int \sum_{i=1}^d \left| \frac{\text{Hu}(\mathbf{k}, \mathbf{r}'; \Psi) - \text{Hu}(\mathbf{k}, \mathbf{r}; \Psi)}{(\mathbf{r}' - \mathbf{r}) \cdot \mathbf{e}_i} \right| \times \exp \left[ \frac{(\mathbf{r}' - \mathbf{r})^2}{2\sigma^2} \right] d^d r', \quad (29)$$

where we sum over the  $d$  orthogonal dimensions each associated with unit vector  $\mathbf{e}_i$ .

Using the Husimi map to measure angular deflection has close ties to its initial introduction as a measurement state for building phase diagrams[2]. For instance, it is possible to use the divergence of the Husimi map for each wavevector to compute the quantum analog of a state's Poincare map[11]. This form of the Husimi map has been used to examine the angle of impact against a coordinate along the boundary[11] to study chaotic behavior in stadium billiards[12, 13].

## III. HUSIMI MAPS IN CLOSED SYSTEMS

### A. Eigenstates of the Circular System

The circular well is an ideal system for demonstrating the Husimi map since their classical dynamics are simple and can be analytically determined.

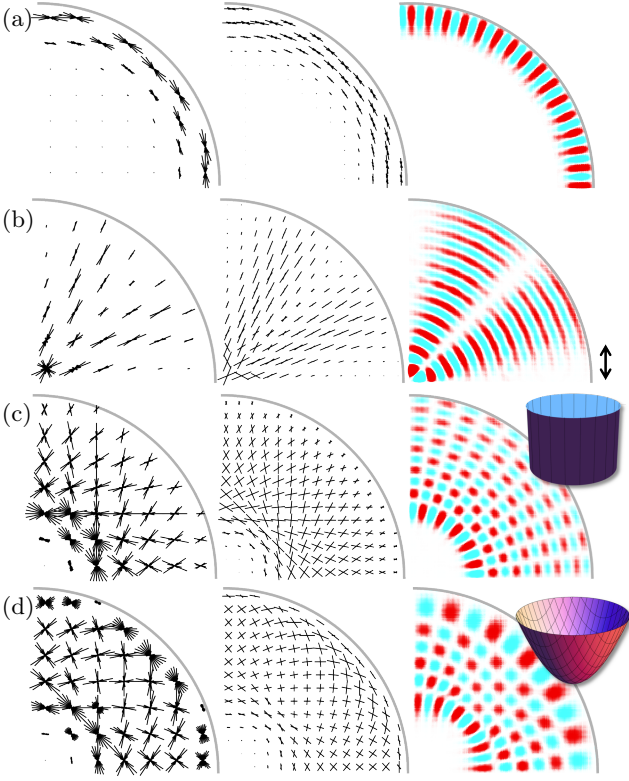


Figure 4: Husimi maps (left), multi-modal analysis (middle), and the wavefunction (right) for eigenstates of the circular well (a-c) and the harmonic oscillator (d). Double-arrows at far right indicate the spread of the coherent state which is  $\Delta k/k = 10\%$ . The states in (c) and (d) correspond to the classical paths in Figs. 5a and b respectively.

The Schrodinger equation can be written in radial form as

$$\frac{d^2 R(r)}{dr^2} + \frac{1}{r} \frac{dR(r)}{dr} + \left( k^2 - \frac{m^2}{r^2} \right) R(r) = 0. \quad (30)$$

Solutions to this equation are simultaneous eigenstates of energy and angular momentum, and thus possess the good quantum numbers  $n$  (number of nodes in the radial direction) and  $m$  (number of angular nodes). Fig. 4a-c shows three such states, the first with  $n = 0$ , the second with  $n \gg m$ , and the third with  $n \approx m$ . The Husimi map in each shows the clear distinction between angular and radial components of the wavefunction, and how they correlate with classical paths with similar properties (further discussion of the classical correspondence can be found in Ref. [14]).

To examine the harmonic oscillator state in Fig. 4d, the Husimi projection at each point must be modified. For the circular well, the dispersion relation is  $\hbar k = \sqrt{2mE}$ , but due to the harmonic potential, it changes to  $\hbar k(\mathbf{r}) = \sqrt{2m(E - V(\mathbf{r}))}$ . This means that a different sweep in  $k$ -space must be made at each point to produce an accurate Husimi map. Fig. 4d shows such a state with  $V(\mathbf{r}) = V_0 r^2$ .

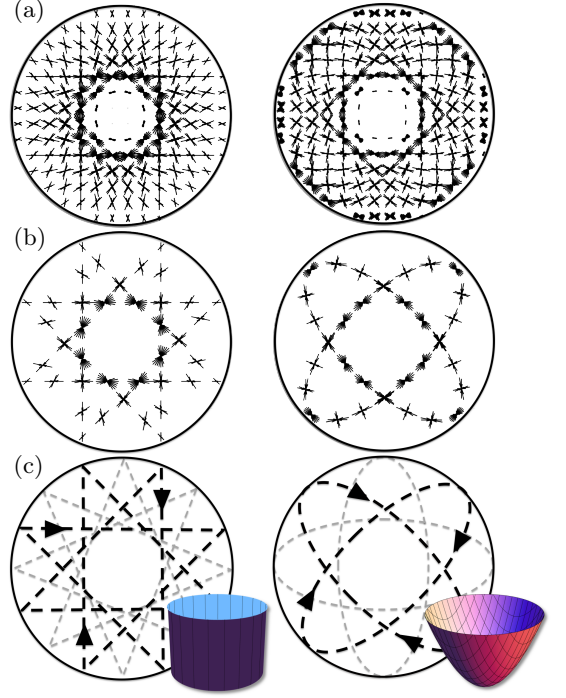


Figure 5: Quantum-classical correspondence from Husimi maps by sampling along classical trajectories. In part (a), the Husimi map for the two eigenstates in Fig. 4c-d, where Husimi projections are sampled along a grid. In part (b), projections are instead sampled along classical paths that correspond to the wavefunction. Because of rotational symmetry, however, the wavefunction is actually created by the sum of many rotations of such paths, as indicated in part (c).

The Husimi vectors in Figs. 4c align to suggest straight trajectories, but the vectors in Fig. 4d do not, suggesting the presence of curved paths. Moreover, projections near the boundaries of both systems indicate that the paths of the circular well bounce off the boundary with a consistent and acute angle, while they graze the edge of the harmonic oscillator.

In this paper, we have chosen to sample the Husimi projections at equally-spaced points along a grid, which makes it possible to compute quantities such as the angular deflection. If we instead sample along one of the classical paths corresponding to the state, we find a set of Husimi vectors which align themselves perfectly with the classical path. We show these two approaches in Figs. 5a and 5b, which correspond to the wavefunctions in Figs. 4c and 4d respectively.

Each Husimi projection in Fig. 5b contains an additional set of Husimi vectors which do not align with the path. These vectors can be understood by considering that wavefunctions for the circular well and harmonic oscillator actually correspond to infinitely many such paths rotated in space due to the circular symmetry of these systems, which we indicate in Fig. 5c. The “cross-hatching” patterns in Fig. 5a-b arise because two

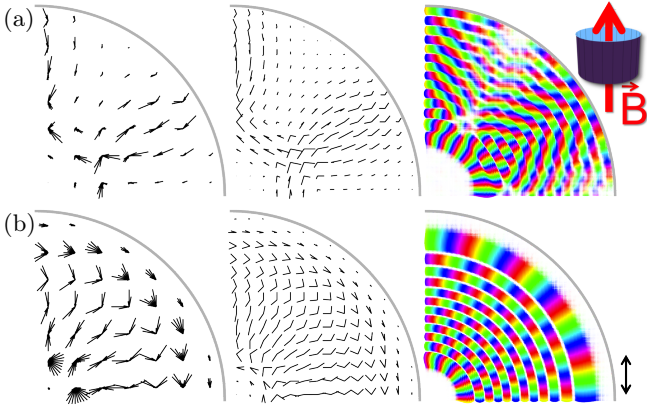


Figure 6: Husimi map (left), multi-modal analysis (middle), and the wavefunction (right) for two eigenstates of the circular well with magnetic field vectors coming out of the plane. The magnetic field strength is set so that the cyclotron radius is approximately  $1/2(a)$  and  $1/3(b)$  of the system radius. Double-arrows at far right indicate the spread of the coherent state which is  $\Delta k/k = 10\%$ . These states correspond to the classical paths discussed in Fig. 7.

rotated classical paths intersect at any point.

Towards the center of the system, a large number of paths come into close proximity. Even though an infinitesimal point is intersected by only two paths, the finite spread of the coherent state is sensitive to other paths nearby, giving rise to Husimi projections showing a large number of trajectories with similar angles. These points in a wavefunction can violate assumptions of the multi-modal analysis in Section IID since the different trajectory angles cannot be resolved by the finite spatial and momentum uncertainties of each Husimi projection. As a result, the multi-modal analysis in Figs. 4c and 4d does not produce the original paths, but their average and approximations on both sides of the average.

## B. Magnetic Field

Systems without time-reversal symmetry can also be studied with the Husimi technique as shown below for systems in the presence of a magnetic field. To properly reflect these states, both the momentum operator in Eq. 1 and the momentum term  $i\mathbf{k}_0 \cdot \mathbf{r}_0$  in Eq. 24 must be modified to reflect the canonical transformation

$$\mathbf{p} \rightarrow \mathbf{p} - q\mathbf{A}/c, \quad (31)$$

where the magnetic potential  $\mathbf{A}$  is defined in App. C.

Results for large magnetic fields, where the cyclotron radius is smaller than the system size (see App. C), are presented in Fig. 6. Unlike the circular well states without magnetic field in Fig. 4, the wavefunctions in Fig. 6 do not exhibit cross-hatching nodal patterns, but circular nodal patterns with complex phase arguments. Projecting each phase argument onto the real axis, however, it is

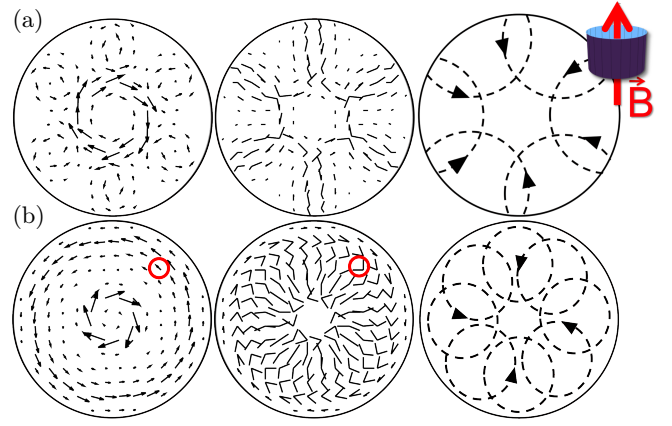


Figure 7: The flux map, multi-modal analysis, and classical paths for the states represented in Fig. 6(a-b). The traditional flux correlates strongly with Husimi flux (Eq. 24) but fails to show the classical paths suggested by the wavefunction. Red circles correspond to magnified views in Fig. 8.

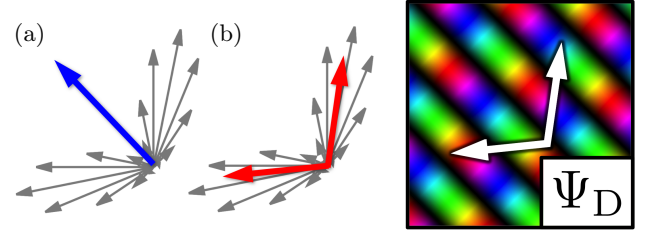


Figure 8: Husimi vectors for 32 equally-space points in  $k$ -space are shown in grey for the double plane waves  $\Psi_D$  defined in Eq. 32. The uncertainty corresponds to  $\Delta k/k = 30\%$ . Because of momentum uncertainty, there is spread in the Husimi vectors. The flux operator (a, blue) averages over the Husimi vectors, while the processed Husimi map (b, red) recovers both underlying wavevectors.  $\Psi_D$  is representative of the areas circled in red in Fig. 7.

easy to see that cross-hatching nodal patterns re-emerge, suggesting the presence of multiple classical trajectories at each point. This intuition is corroborated by the corresponding Husimi maps for each state, which indicate circular classical trajectories with radii corresponding to the cyclotron radius.

In Fig. 7, the full classical paths corresponding to each state are depicted, and correlate strongly with the Husimi map with the canonical transformation. Like the circular well states, the presence of multiple trajectories at each point in Fig. 7 can be explained by the intersection of rotated classical trajectories that arise from rotational symmetry. For the state in Figs. 6a and 7a, we have artificially lifted rotational symmetry to highlight fewer rotated paths.

Because the flux map averages over trajectories at each point, it can often fail to indicate the full classical dynamics underlying a quantum wavefunction. The left column of Fig. 7, which shows the flux map, integrated with a

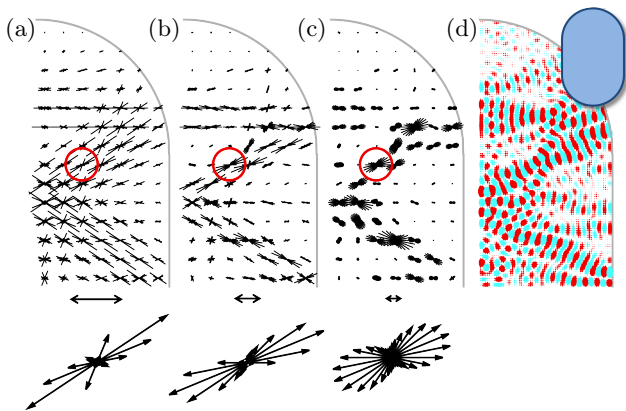


Figure 9: Husimi maps for the scarred stadium billiard eigenstate. Each map uses a different spread of the measurement wavepacket. The spread is indicated by the double-arrows on the bottom, with relative uncertainties of  $\Delta k/k = 5\%$ (a),  $20\%$ (b), and  $50\%$ (c). A single Husimi projection, circled in red, is magnified at the bottom of each representation.

Gaussian kernel corresponding to the coherent state used to generate the Husimi map, is consequently unable to represent the classical paths (right column), but instead measures and total drift flow which might be the desired quantity in some circumstances. In contrast, the multi-modal analysis in the middle column indicates the classical paths with remarkable fidelity.

We can appreciate the difference in detail by examining the areas circled in red in Fig. 7. In Fig. 8, magnified views from the flux operator, multi-modal analysis, and full Husimi map corresponding to these areas are shown. We model this point in the wavefunction according to the pure momentum state

$$\Psi_D(\mathbf{r}) = e^{i\mathbf{k}_3 \cdot \mathbf{r}} + e^{i\mathbf{k}_4 \cdot \mathbf{r}}, \quad (32)$$

where  $\mathbf{k}_3$  and  $\mathbf{k}_4$  are indicated by the white arrows. Not only does the flux average the full Husimi projection, it also averages over the trajectories inferred by multi-modal analysis. As a result, the flux map in the left column Fig. 7 can be deduced from the multi-modal analysis in the middle column by simply summing the vectors at each point.

### C. Stadium Billiard Eigenstates

The classical dynamics of the circular stadium are integrable while those of the Bunimovich stadium[15] are chaotic. As a result, the stadium has been featured in many studies of "quantum chaology"[11, 16–22].

Fig. 9 shows three Husimi maps for a billiard eigenstate. The wavelength at the energy of the eigenstate is much shorter than the size of the system, allowing well-defined scars to form, which are spawned by modestly unstable and infinitely rare (among all the chaotic orbits) classical periodic orbits[1].

For Fig. 9a, an extended coherent state is used to generate the Husimi map, so that many fine features of the wavefunction are washed out. Only the scar path (seen as a rotated "v" pattern in the depiction) is clearly visible. The sharply peaked Husimi sunburst reflects both the low momentum uncertainty of the Gaussian used and the strong dominance of the periodic orbit pathway in the eigenfunction.

Compare this to the Husimi map in Fig. 9c which is generated by a small coherent state with larger momentum uncertainty. Here, each Husimi projection is more ambiguous, and local variations in the wavefunction probability amplitude have a large impact on the representation since they are no longer smoothed over. As a result, the trajectories implied by the map no longer continue from one projection to its neighbors and appear somewhat irregular. In general, a compromise can be made by choosing an intermediate momentum uncertainty, as shown in the Husimi map presented in Fig. 9b. Trajectories are fairly well-resolved, and local variations are easy to follow. Coherent states of this size provide the clearest representation of semiclassical paths.

Even at low energies, where the wavelength is comparable to the size of the system, stadium billiards provide another perspective on the utility of the Husimi map. Unlike the circular system, in which the trajectories adding up at a particular point are fairly regular and predictable, any point in a stadium billiard eigenstate is rife with many unpredictable trajectories. Thus, the Husimi map is an ideal tool for lifting the veil on the underlying classical dynamics.

In Fig. 10, we show Husimi maps for three eigenstates of the closed stadium billiard Hamiltonian. For each calculation, the size of the coherent state is kept constant, but because the energy of the eigenstates increases from top-to-bottom, the momentum uncertainty for each Husimi projection also increases. This is reflected in the clarity of the suggested classical paths at higher energy as well as the reduction of angular deflection in the bulk (which acquires small positive values in the top figure due to uncertainty, not because there is actual deflection at these points).

To the unaided eye, the wavefunctions in Fig. 10 do not appear to emphasize isolated classical trajectories like the high-energy stadium state in Fig. 9, especially since at such low energies the system only accommodates a few wavelengths along its diameter. In the Husimi map, however, it is quite clear that a very limited set of classical trajectories are largely responsible for these wavefunctions, suggesting that Husimi projections could be used to study the properties of low-energy scar states[1].

Points with high angular deflection show which parts of the system boundary are responsible for the creation of each state, and indicate where adiabatic changes in the boundary conditions are most likely to affect the state[23, 24]. This can be imagined as a quantum force on the boundary. Because the size of the coherent state used to generate each Husimi map is kept constant, the angular



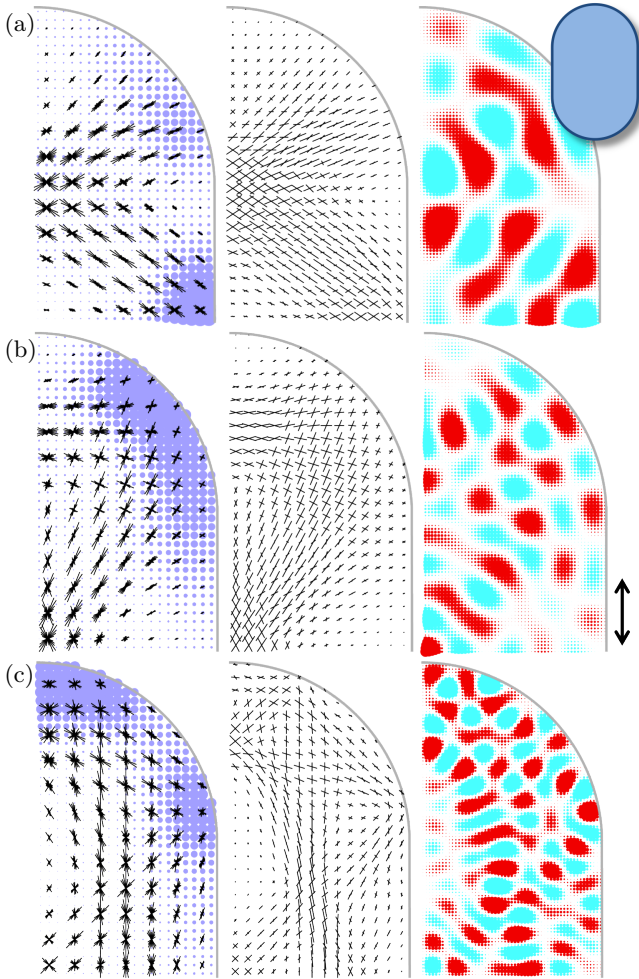


Figure 10: Three eigenstates of the stadium billiard system with Dirichlet boundary conditions at three increasing energies, with the Husimi map (left), multi-modal analysis (middle) and wavefunction (right). Angular deflection is indicated in blue, and the double arrows indicate the test wavepacket spread of  $\Delta k/k = 20\%$ (a),  $15\%$ (b) and  $10\%$ (c).

deflection penetrates into the bulk to the same extent for each state. However, the locations of high angular deflection along the boundary form a unique fingerprint for each state.

## IV. FLUX THROUGH OPEN SYSTEMS

### A. Sub-Threshold Resonance

The previous section used the Husimi map to examine the semiclassical dynamics of closed systems directly from their wavefunctions, providing substantial benefits over the usual flux operator, which vanishes for time reversal symmetric systems, and averages all trajectories (thus missing criss-crossing trajectory paths, see Fig. 7) for a magnetic field present. Moreover, the spread of the

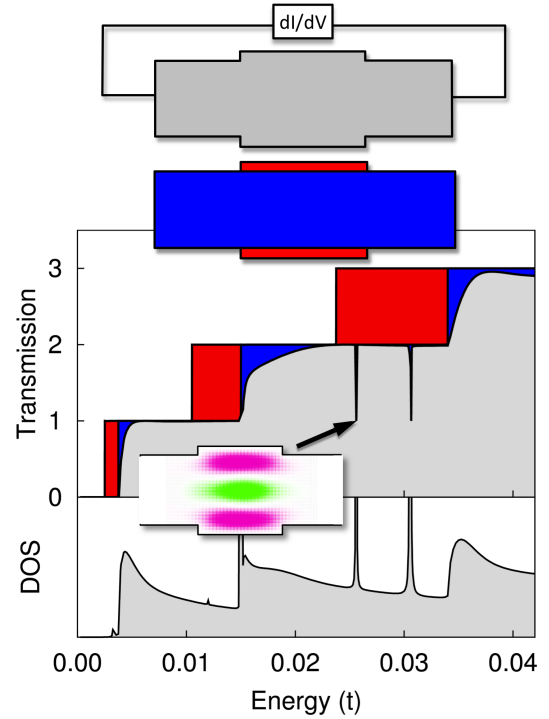


Figure 11: Top: An infinite waveguide schematic with a slight bulge in the middle (grey). This can be modeled as two waveguides of different widths (blue and red). Bottom: In an infinite waveguide, the transmission curve has a series of plateaus as each transverse mode opens up (blue transmission curve). In a wider waveguide, each mode opens up at lower energies (red curve). If only a small segment of the waveguide is widened, then sub-threshold resonances occur in between the energies of the narrow and wide waveguides (grey transmission curve). These correlate with sub-threshold resonant states which peak in the density of states (DOS) at those energies (grey curve). Energy is given in units of  $t$  where  $4t$  is the band edge.

coherent state used to generate the Husimi map gives it the flexibility to examine dynamics at a variety of scales, while the flux operator is confined to the limit of infinitesimal spread. In its traditional guise (Eq. 1), the flux operator is most often employed in scattering problems which arise when a closed system is coupled to an environment. Is it possible to connect the semiclassical dynamics of the closed system to the open system using the extended Husimi flux?

In this section, we demonstrate how the Husimi flux can help interpret the traditional flux and deepen our understanding of transport across a device. We consider sub-threshold resonance for a waveguide that is slightly widened along a short section (see inset, Fig. 11).

In an unperturbed waveguide, transport occurs through transverse modes which open for transport when the system energy exceeds the transverse energy of the mode. At these energies, the transmission function exhibits distinct plateaus as seen in Fig. 11, where the plot



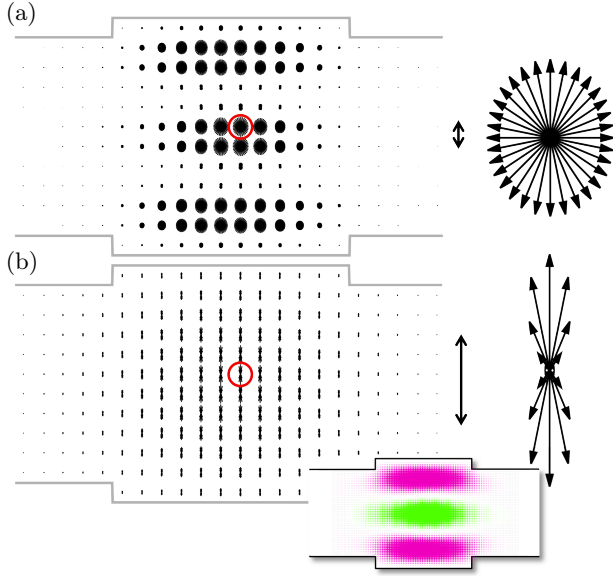


Figure 12: The full Husimi map for the resonant state (see inset) is plotted with  $\Delta k/k = 100\%$  (a) and  $\Delta k/k = 20\%$  (b). The spread of the test wavepacket is indicated by double-arrows. A single Husimi projection (circled in red) for each map is magnified at right. The vector sums of each map are shown in Figs. 14b.

of the transmission for a wide(narrow) waveguide is presented in red(blue).

If a small section of a narrow waveguide is widened, the transverse energy of each mode diminishes in the wider section. Thus, for each mode, there is a range of energies bounded above by its transverse energy in the unperturbed waveguide, and below by its energy in the wider region. In this energy range, the mode can reside in the wider region but cannot propagate through the narrower leads where it is an evanescent wave. This forces it into a quasi-bound state which is trapped in the wider region and is only weakly coupled to the environment, causing a striking peak in the density of states, commonly known as a Feshbach resonance[25]. In the quasi-bound state, the particle bounces vertically between the walls of the perturbed region and is unlikely to escape.

At certain energies, a particle propagating in a lower energy mode corresponding to the narrow section interacts with the wider region and becomes trapped in the quasi-bound state. This causes the quasi-bound state to hybridize with the propagating mode and interfere with the transmission in the device, as seen in Fig. 11. The suppression of transmission appears as a pair of sharp dips, accounting for symmetric and antisymmetric versions of the Feshbach resonance. Since the resulting wavefunction is the hybridized state which inhabits the system at resonance, we refer to it as the resonant state.

We compute the wavefunction of the resonant state corresponding to the first transmission dip in Fig. 11 (indicated by the arrow in the transmission function) according to Appendix D. Our method allows us to extract

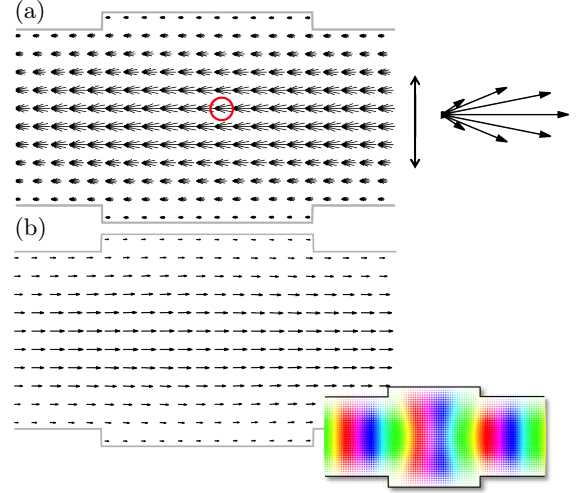


Figure 13: The full Husimi map for lowest propagating mode wavefunction (see inset) from the waveguide in Fig. 11 is plotted in (a), at an energy well above resonance ( $E = 0.02745$  in arbitrary units scaled to Fig. 11). The uncertainty for this map is  $\Delta k/k = 20\%$ . At right, a magnified view of the projection circled in red. In (b), the Husimi flux. This is the mode which hybridizes with the resonant state to produce Figs. 12 and 14.

the pure resonant state without the second-lowest propagating mode, which is also present at these energies. Fig. 12 shows the full Husimi map for this wavefunction, using coherent states with uncertainties of  $\Delta k/k = 100\%$  (a) and  $20\%$  (b). The individual projections correspond strongly to the cosine-wave projections in Fig. 2. Spatial variations in the Husimi map decrease as the size of the coherent state increases, as in Fig. 9.

The full Husimi map is indistinguishable from the quasi-bound state and the resonant state, which is expected since the resonant state only slightly perturbed by the propagating mode. The flux of the quasi-bound state is zero, but exhibits characteristic vortices in the resonant state. Moreover, as the energy is increased across resonance, the wavefunction doesn't substantially change in appearance, while the flux patterns alter dramatically. At first these behaviors appear to contradict the Husimi map, but we can show that the flux patterns correlate with subtle changes in the Husimi maps which we can retrieve by adding all their vectors.

We can begin to understand these subtle changes by examining the lowest propagating mode. The full Husimi map far away from resonance, shown in Fig. 13 for a moderate coherent state, corresponds to the complex plane wave in Fig. 2. In the Husimi flux, the left-to-right flow appears unchanged within the central region of the system. The flux operator for this mode, not shown, is similar. In contrast, the vector-sum and the flux of the bound state is always zero. So what happens when it interacts with the lowest propagating mode to produce the resonant state?

In Fig. 14 we address this question by showing the

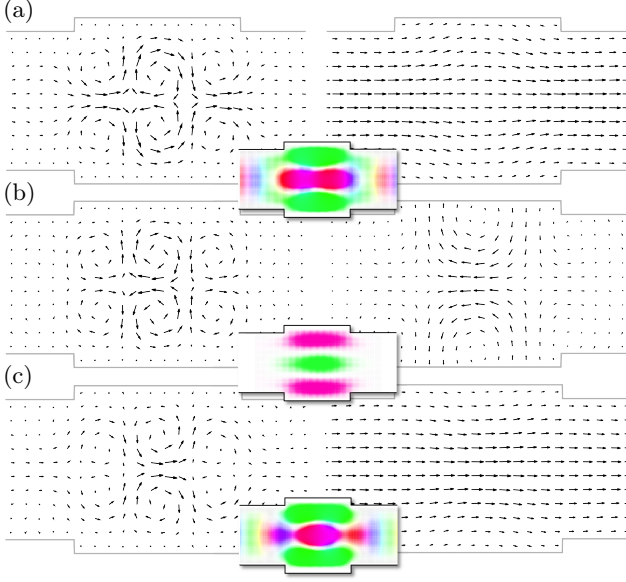


Figure 14: The traditional flux (left column) and the Husimi flux (right column) for the resonance state in Fig. 11 slightly above resonance (a,  $E = E_{\text{res.}} + 0.00005$ ), at resonance (b,  $E = E_{\text{res.}}$ ) and slightly below resonance (c,  $E = E_{\text{res.}} - 0.00005$ ). The coherent state for the Husimi map corresponds to  $\Delta k/k = 0.2$ . The transmission function for this mode at each energy corresponds to  $T = 0.99$ (a),  $0.06$ (b), and  $0.99$ (c). Even though the full Husimi maps at each energy are indistinguishable from Fig. 12, their vector additions (Husimi flux) vary substantially. Energies are in arbitrary units, scaled to Fig. 11.

traditional flux, wavefunction, and the Husimi flux above (a), at (b), and below (c) resonance. The flux operator is integrated over a Gaussian kernel corresponding to a coherent state spread of  $\Delta k/k = 100\%$ , and is visually identical to the Husimi flux with the same coherent state spread.

In the flux operator, we see the characteristic vortex patterns which flip above and below resonance, as expected when the bound state shifts through a phase of  $\pi$  over resonance. Moreover, while it is clear that the presence of the lowest propagating mode is stronger away from resonance, the wavefunction representation at all three energies are strongly influenced by the bound state. Similarly, probability flux is strongly localized in the center of the system, and it is unclear how the vortices correlate with the fact that transmission for this mode goes to zero on resonance.

In the Husimi flux, however, the correlation is obvious. Above and below resonance, vortices cancel out and leave behind the drift velocity of the mode. At these energies, the Husimi flux is quite similar to the lowest propagating mode in Fig. 13, and the left-to-right flow extends through the semi-infinite leads, although there are slight changes in the central region. At resonance, however, the vortices no longer interfere to produce flow from left-to-right, but instead persist as larger vortices

across the central region which counteract the left-to-right flow from the leads, resulting in zero transmission for this mode. The second-lowest propagating mode (not shown), which is antisymmetric along the transverse direction, does not interact with the resonance and maintains full transmission.

At all energies, the full Husimi map shows the simple vertical bouncing trajectories that are identical to the bound state (Fig. 12), while the left-to-right flow of the lowest propagating mode (Fig. 13) interferes with these paths to produce the residual flux vortices. The classical dynamics of the resonance therefore indicate a subtle shift in the overall contribution of classical trajectories which give rise to the resonance. Because the vertical trajectories can easily cancel each other out, the residual becomes exquisitely sensitive to the initial conditions of such classical paths, which are determined solely by the energy of the lowest-propagating mode.

By examining this system using the Husimi flux, which allows us to adjust the coherent state spread arbitrarily, we can zoom into the details of the flux operator at small spreads and pull out to larger drift flows at larger spreads. Important information about the resonance can be retrieved at all scales, since the flow can be understood by the slight residuals of the full Husimi projection with different coherent state spreads. By adding the Husimi projection and the Husimi flux to the analytical toolset, we can examine the problem from all angles to construct a more nuanced and complete story.

## B. Transport Through Other Geometries and the Nature of Flux Vortices

Because the  $\sigma$  parameter defines the spatial spread of the coherent states used to generate a Husimi map, we can use it to reveal the behavior of the probability flux at arbitrary scales. In Fig. 15a, we show the scattering wavefunction that acts as a mode of unit transmission in a large square block geometry. This geometry is changed from the previous subsection so that: 1) Its dimensions are much larger than the characteristic wavelength at the energies we examine, 2) the leads are shifted vertically from the center towards the bottom-left and upper-right, and 3) the center is obstructed to constrain transport through the central region. As a result, classical paths related to transport in this system must reflect off the boundaries many times to propagate from the left to the right lead.

In Fig. 15, we show the wavefunction, a magnified view of the traditional flux, the full Husimi flux, and the multi-modal analysis for this scattering state. In the wavefunction, nodal lines appear to fall along the  $45^\circ$  diagonals, which is corroborated by trajectories favoring those diagonals in the multi-modal analysis. This arises because all boundary conditions are vertical or horizontal walls; since each mode of the unperturbed waveguide leads is associated with a distinct pair of trajectory angles (See

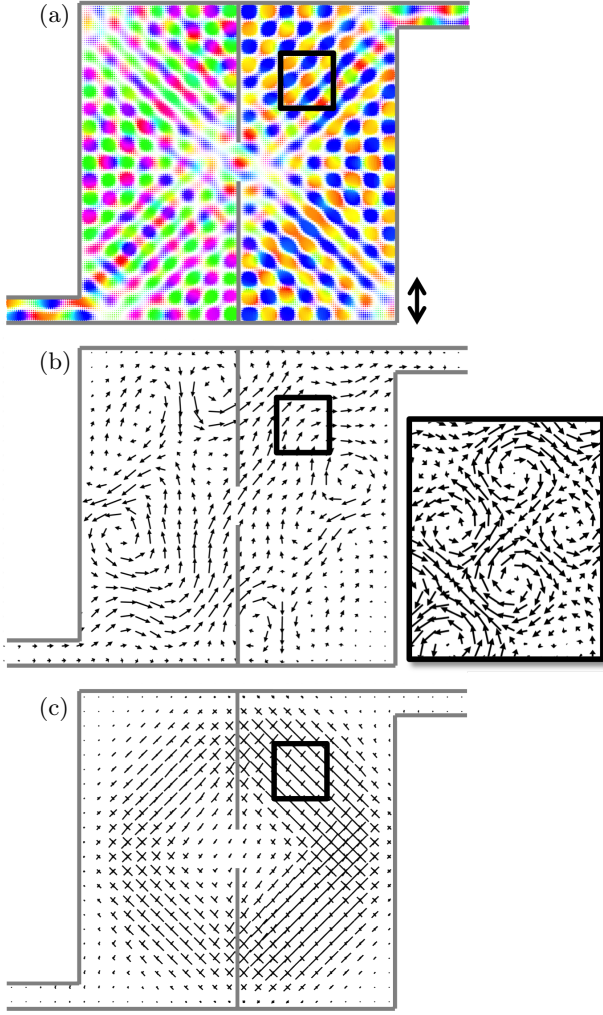


Figure 15: A scattering wavefunction associated with full transmission through the obstructed square with the wavefunction representation (a), the Husimi flux (b) and multi-modal analysis (c) for a coherent state spread of  $\Delta k/k = 10\%$ , indicated by the double arrows. The traditional flux from the part of the system indicated by the black squares is magnified in the inset.

Fig. 16), the vertical and horizontal walls therefore reflect all trajectories back onto the same pair rotated at 45 degrees. At the energy we have selected, the pair of trajectory angles for the incoming mode are at perfect 45° diagonals, so that their rotations from reflecting off the walls also point along the diagonals, giving rise to strong standing waves.

In Fig. 15b, it is clear that transport occurs primarily through a narrow channel we call the conductance pathway with the majority of arrows pointing from the lower-left to the upper-right corners. By comparison, the full traditional flux map (not shown) is rife with vortices throughout the entire system, dramatically limiting our ability to identify overall flow. The conductance pathway does not have to be classical, since it is an aggregate phenomenon from many other classical trajectories; as

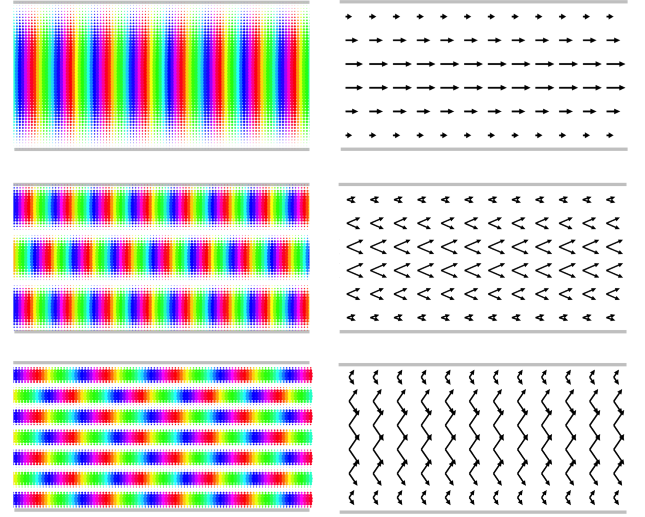


Figure 16: The scattering wavefunction associated with distinct modes of a wide unperturbed waveguide at left, with the multi-modal analysis at right. Each mode is associated with a pair of trajectory angles. As the number of horizontal nodal lines increases, and as energy increases, these angles become increasingly vertical.

a result, it is able to curve in the bulk without external forces, as seen in the figure. As the pathway moves against many other perpendicular classical paths indicated in the multi-modal analysis, pairs of vortices form on either side, which we show in the inset in Fig. 15. These vortex pairs are a direct analog to those which occur in sub-threshold resonance as the left-to-right conductance pathway passes through perpendicular trajectories in the perturbed waveguide (See Fig. 14 and the surrounding discussion).

Fig. 17, examines a full-transmission scattering state for a large half-stadium with two leads attached at its sides. Because scar orbits must self-loop but be otherwise unstable[1], scar states can only participate in transport when the leads attach at points that are slightly displaced from one of the orbit's reflection points; otherwise, the classical orbit leaks out the system too quickly. The wavefunction in Fig. 17 shows strong scarring, and the multi-modal analysis corroborates the scarring with an identifiable classical orbit which just misses the leads.

Like the square device with obstructions in Fig. 15, flux also occurs most strongly along a narrow conductance pathway which, in this case, flows along the bottom of the device while deviating into the bulk at its middle. In addition, flux vortices occur throughout the system, making interpretation difficult without applying our methods. Unlike the square device, however, these vortices no longer form identifiable pairs. In the stadium state, classical paths do not intersect at 90° angles, but take on a variety of other oblique angles. As a result, the vortices take on forms that are consistent with the multi-modal Husimi map at each intersection. For instance, in the black inset, there is strong flow from bottom-left to



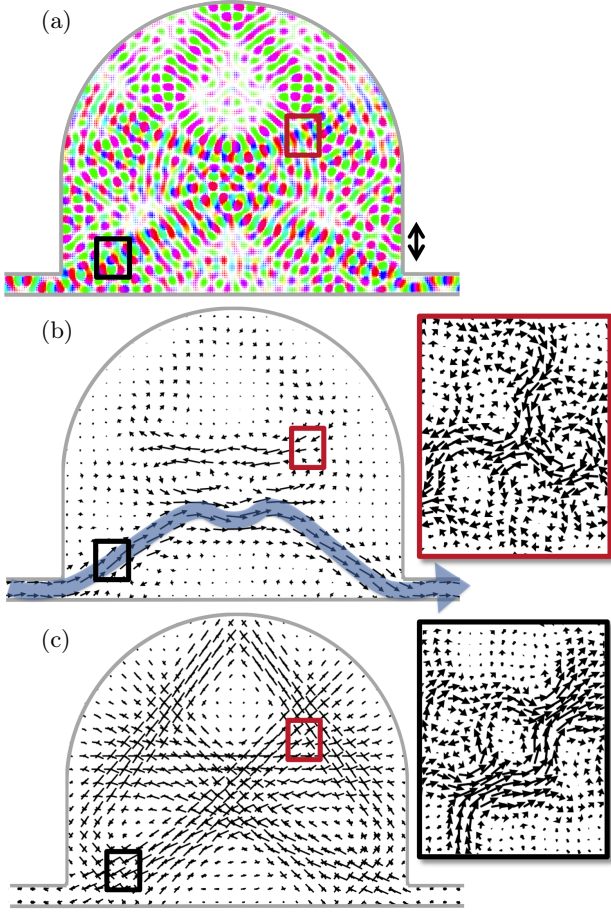


Figure 17: A scattering wavefunction associated with full transmission through the half-stadium in the wavefunction representation (a), the Husimi flux (b) and multi-modal analysis (c) for a coherent state spread of  $\Delta k/k = 10\%$ , indicated by the double arrows. The traditional flux from the part of the system indicated by the black and red squares is magnified in the insets.

upper-right, with other near-vertical flows forming vortices, and in the red inset, there are three primary flows propagating at  $60^\circ$  to each other, forming the triangular arrangement of vortices shown.

## V. CONCLUSIONS

We have extended the definition of the flux operator using a new method for visualizing and analyzing the quantum wavefunction. By using coherent states as a measurement operator built off of the Husimi projection[2] and adapting this technique to generate a vector field, we have shown it is identical to the flux operator for infinitesimal coherent states (Section II B). For finite coherent state spreads, the Husimi projection provides a breakdown of the flux into contributions from dominant classical paths, which can be retrieved by processing our results (Section II D). This technique has proven invaluable

for informing a design principle in quantum systems, since it provides a map of how boundaries affect individual quantum states (Section III C), as well as the impact of potentials (Section 4) and magnetic fields (Section III B). Finally, we have shown its utility for illuminating the many phenomena underlying resonance when a closed system interacts with an environment (Section IV A), while helping to explain the presence and properties of flux vortices (Section IV B). Because of its ability to contextualize the the flux operator and identify the primary conductance pathway in large systems, the Husimi projection is an ideal tool for interpreting quantum conductance simulations.

This paper focuses on two-dimensional systems, since they are ideal for demonstrating the significant physical intuition that the Husimi is able to provide. However, its definition is not limited to such systems. It is equally well suited to three-dimensional systems, and may be able to provide a significant contribution to interpreting molecular orbitals, augmenting such technologies as Bader surfaces analysis[26] and local currents[27].

## Appendix A: Deriving the Expectation Value of the Flux

In this appendix, we show how to derive Eq. 12 from the eigenvalue equation (Eq. 4). We begin by labeling the excited states of the harmonic oscillator at position  $\mathbf{r}_0$  oriented along the  $i^{\text{th}}$  spatial dimension

$$\begin{aligned} \langle \mathbf{r} | 0 \rangle &= \langle \mathbf{r} | \mathbf{r}_0, \sigma \rangle \\ \langle \mathbf{r} | 1 \rangle &= \frac{\mathbf{e}_i \cdot (\mathbf{r} - \mathbf{r}_0)}{\sigma} \langle \mathbf{r} | \mathbf{r}_0, \sigma \rangle \\ \langle \mathbf{r} | 2 \rangle &= \sqrt{\frac{1}{2}} \left( \frac{(\mathbf{e}_i \cdot (\mathbf{r} - \mathbf{r}_0))^2}{\sigma^2} - 1 \right) \langle \mathbf{r} | \mathbf{r}_0, \sigma \rangle \\ &\vdots \end{aligned} \quad (\text{A1})$$

where  $\mathbf{e}_i$  is the unit vector along the  $i^{\text{th}}$  spatial dimension. These states form a complete set in which the flux operator can be explicitly expressed, using a zero-indexed Hermitian matrix, as

$$\hat{j}_{\mathbf{r}_0, \sigma, i} = \begin{pmatrix} 0 & +i\lambda & 0 & \cdots & 0 \\ -i\lambda & 0 & 0 & \cdots & 0 \\ 0 & 0 & 0 & \cdots & 0 \\ \vdots & \vdots & \vdots & \ddots & \vdots \\ 0 & 0 & 0 & \cdots & 0 \end{pmatrix} \quad (\text{A2})$$

where  $\lambda = \lambda_{\sigma, i, +} = \frac{\hbar}{4m\sigma}$ . There are additional sets of harmonic oscillators orthogonal to the above states which are centered at points other than  $\mathbf{r}_0$  also with zero components in the flux matrix

The complete set of eigenstates  $|\lambda_1\rangle, |\lambda_2\rangle, |\lambda_3\rangle, \dots$  of the flux operator expressed in terms of excited states of

the harmonic oscillator are

$$\begin{pmatrix} +1 \\ -i \\ 0 \\ \vdots \end{pmatrix}, \begin{pmatrix} +1 \\ +i \\ 0 \\ \vdots \end{pmatrix}, \begin{pmatrix} 0 \\ 0 \\ 1 \\ \vdots \end{pmatrix}, \dots \quad (\text{A3})$$

with eigenvalues  $-\lambda, \lambda$ , and 0. Measurement by the flux operator collapses the wavefunction onto one of these eigenstates, the infinite majority of which are in the degenerate zero-eigenvalue subspace spanning all excited states of the harmonic oscillator above  $|1\rangle$ . Only the first two eigenstates, confirmed in Eq. 11, yield non-zero flux values, which, as we have already shown, tend towards positive and negative infinity as  $\sigma \rightarrow 0$ .

When expanding the flux expectation value, we can use the complete eigenbasis to show that

$$\begin{aligned} \langle \psi | \hat{j}_{\mathbf{r}_0, \sigma, i} | \psi \rangle &= \left\langle \psi \left| \hat{j}_{\mathbf{r}_0, \sigma, i} \sum_{i=1}^{\infty} |\lambda_i\rangle \right. \right\rangle \left\langle \lambda_i \left| \psi \right. \right\rangle \\ &= \lambda |\langle \psi | \lambda_1 \rangle|^2 - \lambda |\langle \psi | \lambda_2 \rangle|^2. \end{aligned} \quad (\text{A4})$$

From Eq. 11, it can be shown that the contributions from  $|\langle \psi | 0 \rangle|^2$  and  $|\langle \psi | 1 \rangle|^2$  cancel themselves due to the opposite sign of the eigenvalues, and only the cross-term  $\langle \psi | 0 \rangle^* \langle \psi | 1 \rangle - \langle \psi | 0 \rangle \langle \psi | 1 \rangle^*$  remains. This form is directly related to the commonly-found expression of the flux at point  $\mathbf{r}_0$  as

$$\mathbf{j}_{\mathbf{r}_0}(\Psi(\mathbf{r})) = \frac{\hbar}{2mi} (\Psi^*(\mathbf{r}_0) \nabla \Psi(\mathbf{r}_0) - \Psi(\mathbf{r}_0) \nabla \Psi^*(\mathbf{r}_0)). \quad (\text{A5})$$

## Appendix B: Uncertainty Propagation for Husimi Vector Addition

When integrating over the available  $k$ -space in Eq. 24, the resulting Husimi flux vector has lower uncertainty than the individual terms in the integral, but by how much? Understanding this mathematical detail is key to appreciating why the Husimi projection is valuable to extending the flux operator to an operator with defined uncertainty. Moreover, understanding the behavior of uncertainty propagation in this integral makes it possible to confidently approximate the result with a discrete sum, such as the sunbursts in Fig. 2, offering both visual and computational advantages.

We begin by considering the extreme cases. If the wavevector orientation remains unchanged for each measurement, summing up identical measurements has no effect on the final relative uncertainty. On the other hand, when either the spatial coordinates or the wavevectors are sufficiently separated, each Husimi vector constitutes an independent measurement; the uncertainty of the result will reduce by the square root of the number of measurements. In general, calculations fall in between these two extremes.

This analysis is concerned with only one dimension, since the variance along each orthogonal axis can simply be summed. First, the coherent state is expressed in the momentum basis as

$$\langle \mathbf{k} | \mathbf{r}_0, \mathbf{k}_0, \sigma \rangle = \left( \frac{2\sigma}{\sqrt{\pi/2}} \right)^{1/2} \times e^{-\sigma^2(\mathbf{k}-\mathbf{k}_0)^2 + i(\mathbf{k}-\mathbf{k}_0) \cdot \mathbf{r}_0}. \quad (\text{B1})$$

Most generally, the Husimi projection in Eq. 24 is the integral of Husimi functions over all of  $k$ -space. In this appendix, and in the figures throughout this paper, the integral is replaced with a finite sum of test wavevectors  $\{\mathbf{k}_i\}$  which satisfy the dispersion relation at a particular energy.

The variance of the integral in Eq. 24 can be obtained by building on intuition about coherent states. It is well-known that the  $k$ -space variance of the coherent state can be simply derived by integrating the coherent state probability amplitude over  $k$ -space, weighting the integrand by  $(\mathbf{k} - \mathbf{k}_0)^2$ . Using the notation in Eq. B1, this gives  $\sigma_k^2 = \frac{1}{4\sigma_x^2}$  yielding the familiar relation  $\sigma_x \sigma_k = \frac{1}{2}$ . This can be thought of in the Husimi formulation as a statistical result where the quantity  $\sigma_k$  is the variance of each individual term in the Husimi vector summation. In this formulation, the variable is the wavevector and the probability function is the probability amplitude of the coherent state. Because the probability function is complex, we have to take the absolute sum squared.

Factoring in more than one Husimi function into the Husimi projection results in the expression

$$\frac{2\sigma}{\sqrt{\pi/2}} \int_{-\infty}^{\infty} \left| \sum_i (k - k_i) e^{-\sigma^2(k-k_i)^2 + i(k-k_i)x_0} \right|^2 dk, \quad (\text{B2})$$

where the set  $\{\mathbf{k}_i\}$  are the set of test wavevectors, projected onto the given axis,  $x_0$  is the spatial point being tested, and  $\sigma$  is the chosen spatial Gaussian spread. Setting the coherent states to the same phase at their centers,  $x_0 = 0$ , and the above integral can be evaluated to return

$$\sigma_k^2 = \frac{1}{4\sigma^2} \left( N + 2 \sum_{i,j>i} e^{-\frac{\sigma^2}{2}(k_i-k_j)^2} \left( 1 - \sigma^2(k_i-k_j)^2 \right) \right). \quad (\text{B3})$$

Already it is possible test this result against intuition. If each wavevector is identical, then  $k_i - k_j = 0$  and the sum of  $N$  measurements results in the uncertainty  $\sigma_k^2 = \frac{N^2}{4\sigma^2}$  which would provide no reduction of relative uncertainty. For large values of  $|k_i - k_j| \gg \sigma$ , the exponential term will overwhelm the quadratic term and the uncertainty becomes  $\sigma_k^2 = \frac{N}{4\sigma^2}$ , a reduction in the relative uncertainty of  $\sqrt{N}$ .

Perhaps most surprising about Eq. B3 is that the second term, which quantifies the covariance between the two measurements, can actually be negative. What are



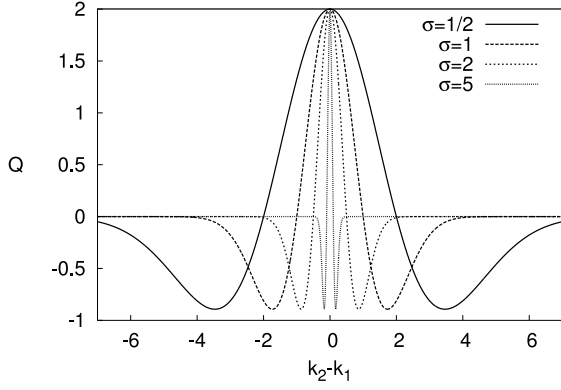


Figure 18: The second term in Eq. B3 is plotted for the addition of two vectors in the Husimi projection. This term represents the covariance between the two vectors, and is bounded above by 2 and below by  $-\frac{4}{e^{3/2}}$  for all choices of  $\sigma$ .

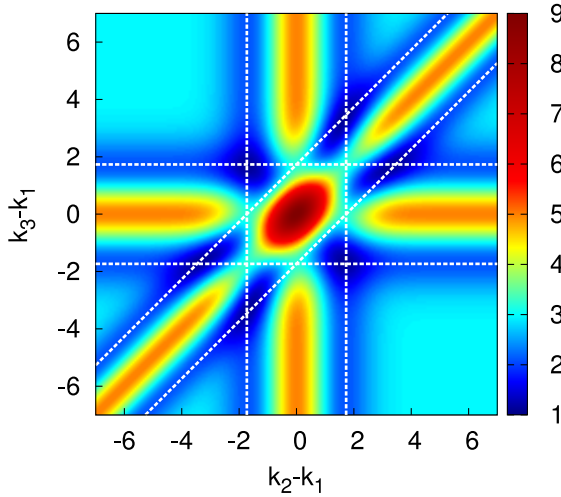


Figure 19: The uncertainty that results from summing three vectors of a Husimi projection, as written in Eq. B3 is plotted. The uncertainty is bounded above by  $9/4\sigma^2$  and below by  $\sim 1.017/4\sigma^2$ . The dashed white lines indicate local minima that result from spacing each pair of vectors by  $\sqrt{3}/\sigma$ , which would give a minimum uncertainty for two-vector addition (see Fig. 18).

its bounds? Fig. 18 plots the quantity  $Q(k_1, k_2, \sigma) = 2e^{-\frac{\sigma^2}{2}(k_2 - k_1)^2} (1 - \sigma^2(k_2 - k_1))$ , showing that a minimum value of  $-\frac{4}{e^{3/2}} \approx -0.893$  is achieved at  $|k_2 - k_1| = \sqrt{3}/\sigma$ . Every value of  $|k_2 - k_1|$  beyond which  $Q$  goes through zero has achieved nearly independent measurements, which is found at  $|k_2 - k_1| = \sigma^{-1}$ .

The terms in Eq. B3 suggest that when more and more vectors are added the uncertainty can be reduced arbitrarily by setting the correct separations between the test wavevectors. It even suggests that for three or more vectors we could possibly produce results with negative uncertainty, but intuitively that cannot be possible. To appreciate why from an analytical perspective, Fig. 19 plots the results of  $\sigma_k^2$  for the addition of three wavevec-

tors. The minima that occur from maximizing the separation between each pair of wavevectors is indicated by the white dashed lines. At the center of the graph, a peak exists at  $\sigma_k^2 = 9/4\sigma^2$ , which falls to  $3/4\sigma^2$  for areas beyond the area bounded by the white dashed lines, consistent with earlier observations. There is also a minimum (positive) uncertainty which arises from the fact that the separation between all pairs of points on a line cannot be equal. In Fig. 19 this is evidenced by the fact that there are no points where three dashed lines intersect. For two vectors the minimum occurs at  $\sigma_k^2 \approx 0.981/4\sigma^2$ , for three  $\sigma_k^2 \approx 1.017/4\sigma^2$  and for four  $\sigma_k^2 \approx 1.036/4\sigma^2$ . We can generalize and state that for  $N_{\min}$  vectors that fall on separate minima, the uncertainty of their sum will be  $\sigma_k \approx \frac{1}{2N_{\min}\sigma}$ .

Moreover, even if vectors are added that do not fall on the uncertainty minima in Figs. 18 and 19, they will have a negligible impact on the total relative uncertainty. So no matter how many vectors contribute to the sum, only the vectors on the minima will reduce the relative uncertainty, making the key quantity not the total number of vectors that are added, but the number that have sufficient separation to fall on the uncertainty minima.

How many vectors is this? We know, for instance, that this minimum occurs when the maximum number of vector pairs have a separation near  $\sqrt{3}/\sigma$ , and that this is likely to occur when they are evenly spaced on a line at that separation. Thus we propose that the number of vectors that can fall on the minima is given by  $N_{\min} = \text{floor}(2k(E)\sigma/\sqrt{3})$ , and using  $\hbar k = \sqrt{2mE}$ , we can rewrite this as  $N_{\min} = \text{floor}\left(\sigma\sqrt{\frac{8mE}{3\hbar^2}}\right)$ . Substituting this value results in the proportionalities

$$\Delta k/k \propto \frac{1}{N_{\min}\sigma} \propto \left(\frac{\sigma}{\hbar}\sqrt{mE}\right)^{-1}. \quad (\text{B4})$$

This makes sense intuitively: the relative uncertainty of a finely sampled Husimi vector addition goes down with larger  $\sigma$  and energy.

This result deepens the connection between the flux operator and the Husimi function for small  $\sigma$ , since for very small coherent states, the uncertainty minima, which are separated by  $\sigma^{-1}$ , grow increasingly far apart. There is only a finite range of wavevectors which satisfy the dispersion relation at a given energy, meaning that as the coherent states get smaller, fewer and fewer samples in  $k$ -space minimize the uncertainty. In fact, at the extreme limit of  $\sigma \rightarrow 0$ , the uncertainty cannot be minimized beyond a single measurement in each orthogonal direction, indicating that results for these small coherent states have undefined uncertainty, just like the flux operator. We corroborate this result using a different proof in Eq. 20.

### Appendix C: The Hamiltonian

Numerical simulations in this paper use a free-particle Hamiltonian  $H = -\frac{p^2}{2m} + U(\mathbf{r})$  sampled on a square grid with spacing  $a$  and where  $U(\mathbf{r}) = 0$  at all points unless otherwise stated. This Hamiltonian can be expressed in more familiar language by using the tight-binding approximation. In this approximation, the effective mass envelope function Hamiltonian becomes  $H = \sum_i \epsilon_i \mathbf{a}_i^\dagger \mathbf{a}_i - t \sum_{\langle ij \rangle} \mathbf{a}_i^\dagger \mathbf{a}_j$  where  $\mathbf{a}_i$  is the annihilation operator for the  $i^{\text{th}}$  grid point,  $\epsilon_i$  is the energy of the system plus the disorder potential, and the set  $\langle ij \rangle$  cycles through all nearest-neighbor pairs. This gives the hopping term  $t = \frac{\hbar^2}{2ma^2}$  and  $\epsilon_i = 4t + U_i$ , where  $U_i$  is everywhere zero unless otherwise stated.

Sec. IIIB uses the Peierls substitution[28] to incorporate magnetic fields, using the language of the tight-binding model. In this model, the magnetic field contributes a phase to the hopping potential  $t$ :

$$t_{ij} = t \exp[i\phi], \phi = q\mathbf{A} \cdot (\mathbf{r}_i - \mathbf{r}_j)/\hbar, \quad (\text{C1})$$

where  $\mathbf{r}_i$  is the position vectors of the site corresponding to the  $i^{\text{th}}$  column of the Hamiltonian,  $\hbar$  is Planck's constant, and  $q$  is the electron charge. Calculations in this paper assume that the magnetic field is perpendicular to the plane on which the system sits and is bounded by a cylinder centered on the system's center. The radius of this column is chosen to be greater than the size of the system. Accordingly, the gauge of the magnetic potential for an out-of-plane magnetic field is defined such that

$$\mathbf{A}(\mathbf{r}) = \frac{e_\theta}{2\pi r} \int B_z dx dy, \quad (\text{C2})$$

where the integral is over a disc centered on the origin and limited by radius  $r$ .

The cyclotron radius can be determined by the relation

$$r = \frac{\hbar k}{B_0 q}. \quad (\text{C3})$$

For a free particle,  $\hbar k = \sqrt{2mE}$ , giving

$$\frac{r}{a} = \frac{\sqrt{2mE}}{B_0 q a^2}. \quad (\text{C4})$$

This means that at  $E = 0.2 \frac{\hbar^2}{ma^2}$ , the energy used in Sec. IIIB, a magnetic field strength of  $B_0 = 2 \times 10^{-3} \frac{\hbar}{qa^2}$  is sufficient to produce a cyclotron radius that is 2/3 of the system radius. This relation is used to predict the cyclotron radius for all calculations in this paper.

### Appendix D: Scattering Wavefunctions

Diagonalizing the Hamiltonian to examine eigenstates of a closed system is straightforward. Sec. IVA, however, examines an open system in a standard ballistic

conductance calculation. The numerical Green's function formalism is used to obtain the scattering wavefunction for these calculations, for which modern implementations are outlined in several texts[29–31]. In this formalism, the Hamiltonian is divided into a left-lead, central region, and right-lead projections

$$H = \begin{pmatrix} H_L & V_{LC} & 0 \\ V_{LC}^\dagger & H_C & V_{RC} \\ 0 & V_{RC}^\dagger & H_R \end{pmatrix}. \quad (\text{D1})$$

The semi-infinite Green's function at the surface of each lead is calculated using the Lopez-Sancho's method, written it as  $g_{L,R}(E)$  for the left ( $L$ ) and right ( $R$ ) leads, which are both equal. To compute the Green's function for the infinite system within the device  $G(E)$  the semi-infinite surface Green's functions  $g(E)$  for each lead[32, 33] are first computed and matched to the surface Green's function of the device region, using the numerical technique outlined in Mason et al.[34].

The coupling matrix for the left lead to the central region is then defined by  $\Gamma_L(E) = 2\text{Im} [V_{LC}^\dagger g_L(E) V_{LC}]$ . This results in a density matrix of coherent scattering wavefunctions  $\rho = G\Gamma_L G$  where we have dropped the implicit energy dependence. Each coherent scattering wavefunction in the system can be obtained by diagonalizing  $\rho$ . Associated with each eigenvector of  $\rho$  will be an eigenvalue equal to the likelihood of measuring the wavefunction within the system. Since there are generally more basis sets within the central region than modes available to the system through the semi-infinite leads, the vast majority of the eigenvalues will be zero, and the number of non-zero eigenvalues will be equal to the number of modes available to the system at the given energy. This number determines the maximum transmission across the central region.

Since a resonant state “traps” the wavefunction at a specific energy, it creates a striking peak in the density of states (see Fig. IVA). As a result, the resonant state can be easily identified among the eigenvectors of the density matrix since it will be associated with the largest eigenvalue near the resonance energy. When discussing resonant wavefunctions, it will be assumed that we are using a density matrix near the resonance energy and examining the eigenvector associated with the largest eigenvalue (and measurement probability) at that energy. This makes it possible to distinguish the resonant wavefunction from other modes which are propagating through the system but are unaffected by the resonance.

### Acknowledgments

This research was conducted with funding from the Department of Energy Computer Science Graduate Fellowship program under Contract No. DE-FG02-97ER25308.

MFB and EJH were supported by the Department of En-

ergy, office of basic science (grant DE-FG02-08ER46513).

- 
- [1] Eric J. Heller. Bound-state eigenfunctions of classically chaotic hamiltonian systems: Scars of periodic orbits. *Phys. Rev. Lett.*, 53(16):1515–1518, Oct 1984.
  - [2] K. Husimi. Some formal properties of the density matrix. *Proc. Phys. Math. Soc. Jpn.*, 22:264–314, 1940.
  - [3] Douglas J. Mason, Mario F. Borunda, and Eric J. Heller. A semiclassical interpretation of probability flux. *arXiv*, 2012.
  - [4] W. Gale, E. Guth, and G. T. Trammell. Determination of the quantum state by measurements. *Phys. Rev.*, 165:1434–1436, Jan 1968.
  - [5] Yakir Aharonov and Lev Vaidman. Measurement of the schrödinger wave of a single particle. *Physics Letters A*, 178:38 – 42, 1993.
  - [6] M. Daumer, D. Dürr, S. Goldstein, and N. Zanghi. On the quantum probability flux through surfaces. *Journal of Statistical Physics*, 88:967–977, 1997.
  - [7] E. J. Heller. Wavepacket dynamics and quantum chaology. In M. J. Giannoni, A. Voros, and J. Zinn-Justin, editors, *Proceedings of the 1989 Les Houches Summer School on “Chaos and Quantum Physics”*, pages 546–663, North-Holland, 1989. Elsevier Science Publishers B.V.
  - [8] P.W. O’Connor and S. Tomsovic. The unusual nature of the quantum baker’s transformation. *Annals of Physics*, 201(1):218–264, 1991.
  - [9] M.S. Child, G. Bruun, and R. Paul. Short time quantum phase space dynamics at a 1:2 fermi resonance. *Chemical Physics*, 190:373 – 380, 1995. Overtone Spectroscopy and Dynamics.
  - [10] Andrea Damascelli. Probing the electronic structure of complex systems by arpes. *Physica Scripta*, 2004(T109):61, 2004.
  - [11] M.C. Gutzwiller. *Chaos in classical and quantum mechanics*. Interdisciplinary applied mathematics. Springer-Verlag, 1990.
  - [12] L. Kaplan and E. J. Heller. Measuring scars of periodic orbits. *Phys. Rev. E*, 59(6):6609–6628, Jun 1999.
  - [13] W. E. Bies, L. Kaplan, M. R. Haggerty, and E. J. Heller. Localization of eigenfunctions in the stadium billiard. *Phys. Rev. E*, 63:066214, May 2001.
  - [14] R. W. Robinett. Visualizing the solutions for the circular infinite well in quantum and classical mechanics. *American Journal of Physics*, 64(4):440–446, 1996.
  - [15] L. A. Bunimovich. On the ergodic properties of some billiards. *Funct. Anal. App.*, 8:73–74, 1974.
  - [16] M. V. Berry. The bakerian lecture, 1987: Quantum chaology. *Proceedings of the Royal Society of London. A. Mathematical and Physical Sciences*, 413(1844):183–198, 1987.
  - [17] Patrick W. O’Connor and Eric J. Heller. Quantum localization for a strongly classically chaotic system. *Phys. Rev. Lett.*, 61:2288–2291, Nov 1988.
  - [18] Michael V Berry. Quantum chaology, not quantum chaos. *Physica Scripta*, 40(3):335–336, 1989.
  - [19] S. Sridhar and E. J. Heller. Physical and numerical experiments on the wave mechanics of classically chaotic systems. *Phys. Rev. A*, 46:R1728–R1731, Aug 1992.
  - [20] Steven Tomsovic and Eric J. Heller. Long-time semiclassical dynamics of chaos: The stadium billiard. *Phys. Rev. E*, 47:282–299, Jan 1993.
  - [21] Fernando P. Simonotti, Eduardo Vergini, and Marcos Saraceno. Quantitative study of scars in the boundary section of the stadium billiard. *Phys. Rev. E*, 56:3859–3867, Oct 1997.
  - [22] Alex Barnett, Doron Cohen, and Eric J. Heller. Deformations and dilations of chaotic billiards: Dissipation rate, and quasiorthogonality of the boundary wave functions. *Phys. Rev. Lett.*, 85:1412–1415, Aug 2000.
  - [23] Alex Barnett, Doron Cohen, and Eric J. Heller. Deformations and dilations of chaotic billiards: Dissipation rate, and quasiorthogonality of the boundary wave functions. *Phys. Rev. Lett.*, 85:1412–1415, Aug 2000.
  - [24] Doron Cohen, Alex Barnett, and Eric J. Heller. Parametric evolution for a deformed cavity. *Phys. Rev. E*, 63:046207, Mar 2001.
  - [25] Herman Feshbach. Unified theory of nuclear reactions. *Annals of Physics*, 5(4):357 – 390, 1958.
  - [26] R F W Bader. *Atoms in Molecules: a Quantum Theory*. New York: Oxford University Press, 1990.
  - [27] Gemma C. Solomon, Carmen Herrmann, Thorsten Hansen, Vladimiro Mujica, and Mark A. Ratner. Exploring local currents in molecular junctions. *Nat Chem*, 2(3):223–228, 03 2010.
  - [28] R. Peierls. Zur theorie des diamagnetismus von leitungselektronen. *Zeitschrift für Physik A Hadrons and Nuclei*, 80:763–791, 1933. 10.1007/BF01342591.
  - [29] S. Datta. *Electronic Transport in Mesoscopic Systems*. Cambridge University Press, Cambridge, 1997.
  - [30] S. Datta. *Quantum transport: atom to transistor*. Cambridge University Press, 2005.
  - [31] D.K. Ferry and S.M. Goodnick. *Transport in nanostructures*. Cambridge Studies in Semiconductor Physics and Microelectronic Engineering. Cambridge University Press, 1999.
  - [32] M. P. López-Sancho and J. Rubio. Quick iterative scheme for the calculation of transfer matrices: application to mo (100). *J. Phys. F.: Met. Phys.*, 14:1205–1215, 1984.
  - [33] M. P. López-Sancho and J. Rubio. Highly convergent schemes for the calculation of bulk and surface green functions. *J. Phys. F.: Met. Phys.*, 15:851–858, 1985.
  - [34] Douglas J. Mason, David Prendergast, Jeffrey B. Neaton, and Eric J. Heller. Algorithm for efficient elastic transport calculations for arbitrary device geometries. *Phys. Rev. B*, 84:155401, Oct 2011.